Inorganic Chemistry

Article

pubs.acs.org/IC

Impact of Cu Doping on the Structure and Electronic Properties of $LaCr_{1-y}Cu_yO_3$

Ilyas Qasim, Peter E. R. Blanchard, Samuel Liu, and Brendan J. Kennedy*

School of Chemistry, The University of Sydney, Sydney, New South Wales 2006, Australia

Maxim Avdeev

Australian Nuclear Science and Technology Organisation, Lucas Heights, New South Wales 2234, Australia

Supporting Information

ABSTRACT: Oxides of the type $LaCr_{1-y}Cu_yO_3$ have been prepared using solid-state methods and their crystal structures refined using synchrotron X-ray powder diffraction. The solubility limit of Cu was found to be around y = 0.2, and such oxides are orthorhombic in space group *Pbnm*. X-ray absorption spectroscopy measurements at the Cr and Cu L-edges demonstrated that the Cr remains trivalent upon Cu doping, with the Cu being present as Cu(III). The oxides are found to be antiferromagnets, and the Néel temperature, T_N, decreases as the Cu content is increased. The crystal and magnetic structures of one example $La(Cr_{0.85}Cu_{0.15})O_3$ have been investigated between 3 and 350 K by neutron powder diffraction. The samples are semiconductors.

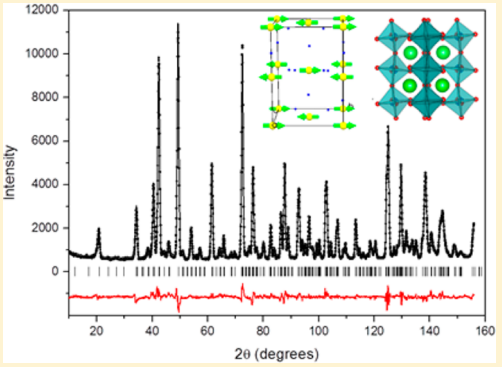

INTRODUCTION

The perovskite structure exhibits considerable flexibility, enabling a wide selection of elements to be incorporated therein. Such substitutions drive structural distortions that can have a significant impact on the magnetic and electronic properties and the interplay between the two. Understanding the relationship between the structure and the properties is a major goal of contemporary inorganic chemistry. This flexibility also sees perovskites being developed for a range of applications including use in ferroelectrics, magnetic devices, and microelectronics, such as memory devices, capacitors, electronic filters, and resonators, etc. Conducting ceramic oxides have been identified as candidates for use in solid oxide fuel cells (SOFCs), and numerous perovskites are been investigated for this purpose. SOFCs are of considerable current interest for use under a range of conditions from transportation to medium-scale power generation due to their, perceived, environmental friendliness, high efficiency, long-term stability, fuel flexibility, and relatively low cost. The high operating temperature (500–1000 °C) of SOFCs presents major materials challenges for both the electrodes and the interconnects.[1−4]

The magnetic and structural properties of the perovskite lanthanum chromite $LaCrO_3$ are also of interest. Pure $LaCrO_3$ is a G-type antiferromagnet (AFM) with a Néel temperature around 300 K.[5−7] Recent studies of the series $LnCrO_3$ (Ln is a lanthanoid from La to Lu) by Zhou and co-workers[8] suggest that distortions of the structure are closely related to dramatic changes in the magnetic ordering temperature. Doping $LaCrO_3$ with Ti alters the Néel temperature, but the magnetic structure remains the same.[9] It has an orthorhombic $GdFeO_3$-type structure at room temperature with space group *Pbnm* (No. 62)[10−12] and undergoes a first-order orthorhombic to rhombohedral structural transition at about 530 K.[11−13] The rhombohedral form is stable to high temperatures, and it appears that it persists to above 1870 K.[13−15]

$LaCrO_3$ is a *p*-type electronic conductor[16] and has a high melting point (above 2400 °C).[17] It is chemically stable, and its thermal expansion is compatible with the most commonly employed SOFC electrolyte material, ionic conducting yttria-stabilized zirconia (YSZ), over a wide temperature range.[18] These properties make $LaCrO_3$ a promising material for use as both electrode and interconnect material in SOFCs.[1−3,19−21] However, the electrical conductivity of pure $LaCrO_3$ is not sufficiently high for use as an interconnect in SOFCs, although both can be increased by substituting acceptor-type larger divalent cations such as calcium and strontium at the *A* site of the $LaCrO_3$;[20−26] however, poor sinterability remains a major issue.[1,19,27] Compared to *A*-site doping relatively less attention has been directed toward studies of *B*-site-doped materials $LaCr_{1-y}B_yO_3$.[7,24,28]

Partial replacement of the Cr by a divalent metal requires partial oxidation of the Cr, formation of oxygen vacancies, or both, in order to maintain charge neutrality. While often considered an attractive manner to tune the properties of perovskite oxides, aliovalent substitution can place a limit on

Received: November 26, 2013
Published: January 31, 2014

   dx.doi.org/10.1021/ic402927y | *Inorg. Chem.* 2014, 53, 2240−2247

the stability of the structure. Alternatively, electronic effects such as the Jahn−Teller distortion common for Mn^{3+} can impact the structure and stability of the oxides as evident from recent studies of $Sr_{1-y}Ce_yMnO_3$, although recent studies of $LaCr_{1-y}Mn_yO_3$ oxides reported that for Mn doping up to y = 0.3 there was minimal impact on the crystal and magnetic structures.[7,29−31] Another Jahn−Teller active cation is the $3d^9$ Cu^{2+} cation. In the present study we examine the impact of Cu doping on the structure and magnetic properties of $LaCrO_3$ and show that charge balance is achieved by oxidation of the Cu rather than Cr.

EXPERIMENTAL SECTION

Polycrystalline samples of $LaCr_{1-y}Cu_yO_3$ (y = 0, 0.05, ..., 0.3) were prepared by a conventional solid-state reaction using La_2O_3, Cr_2O_3, and CuO as starting materials. The reagents were finely mixed as an acetone slurry in an agate mortar and pestle before being heated in air at 1000 °C for 12 h and 1200 °C for 48 h with regrinding and pelletizing before every heating step. After a final regrinding, the $y \geq$ 0.2 samples were heated at 1350 °C whereas the other samples were annealed at 1300 °C for 96 h with an intermediate grinding and pelletizing. All samples were furnace cooled down to around 100 °C at an approximate cooling rate of 4 °C/min. The progress of all reactions was monitored by ex-situ powder X-ray diffraction with Cu Kα radiation using a PANalytical X'Pert PRO X-ray diffractometer equipped with a PIXcel solid-state detector. When the X-ray diffraction patterns no longer changed and showed no detectable impurities, the synthesis was considered to be complete. The structures were refined by the Rietveld method from synchrotron X-ray diffraction (SXRD) patterns recorded using the powder diffractometer at BL-10 of the Australian Synchrotron.[32] Data were collected at room temperature in an angular range of $5° \leq 2\theta \leq 85°$ using X-rays of wavelength of 0.82554 Å, calibrated against NIST SRM660a LaB_6. Each finely ground sample was placed in a 0.3 mm diameter capillary that was rotated during the measurements. The Rietveld method, as implemented in the program Rietica,[33] was used in the final stages of data analysis.

Neutron powder diffraction (NPD) data were collected on the high-resolution diffractometer Echidna at the OPAL facility (Lucas Heights, Australia) using neutrons of wavelength 1.6215 Å.[34] The powder sample was loaded into a vanadium can, and data were collected between 3 and 350 K using a closed-cycle cryostat. Rietveld analysis of the data was performed using the program GSAS[35] employing the default neutron scattering lengths and Cr^{3+} magnetic form factor.

Cr and Cu L-edge X-ray absorption near edge structure (XANES) spectra were collected on the Soft X-ray Spectroscopy beamline at the Australian Synchrotron.[36] Powder samples were lightly dusted on double-sided carbon tape (SPI Supplies) and inserted into the vacuum chamber via a load lock. Pressure inside the analysis chamber was maintained at better than $\sim 1 \times 10^{-9}$ Torr. Cr L-edge XANES spectra were collected from ~20 eV below to ~40 eV above the Cr L_3-edge absorption edge. Cu L-edge XANES spectra were collected between ~30 eV below and ~70 eV above the Cu L_3-edge absorption edge. Spectra were collected in both total electron (TEY) and total fluorescence (TFY) yields with a step size of 0.1 eV and a dwell time of 1 s. All spectra were taken simultaneously with a TEY signal measured from a standard metal reference foil in the beamline. This reference foil removed approximately 10% of the beam intensity. The Cr L-edge was calibrated against Cr metal with the maximum of the first derivative set to 574.1 eV.[37] The Cu L-edge was calibrated against Cu metal with the maximum of the first derivative set to 932.7 eV.[37] All spectra were analyzed using the Athena software package.[37]

Magnetic susceptibility and electrical resistivity were measured with a Quantum Design Physical Property Measurement System (PPMS) system in the range of 5−300 K. Zero-field-cooled (ZFC) and field-cooled (FC) magnetic susceptibility data were collected with a magnetic field of 1000 Oe. The microstructure and homogeneity of the samples was examined by scanning electron microscopy using a Zeiss EVO50 SEM. The average cationic composition for each sample was verified by energy-dispersive X-ray spectroscopy (EDS) using the same microscope; in all cases the measured values were consistent with the nominal compositions.

RESULTS AND DISCUSSION

Microscopic and Compositional Analysis (SEM-EDS). SEM images for various $LaCr_{1-y}Cu_yO_3$ samples are displayed in Figure 1. Although difficult to quantify, the crystallinity of the samples appears to increase with increasing Cu amount, with the y = 0.15 sample appearing the most crystalline.

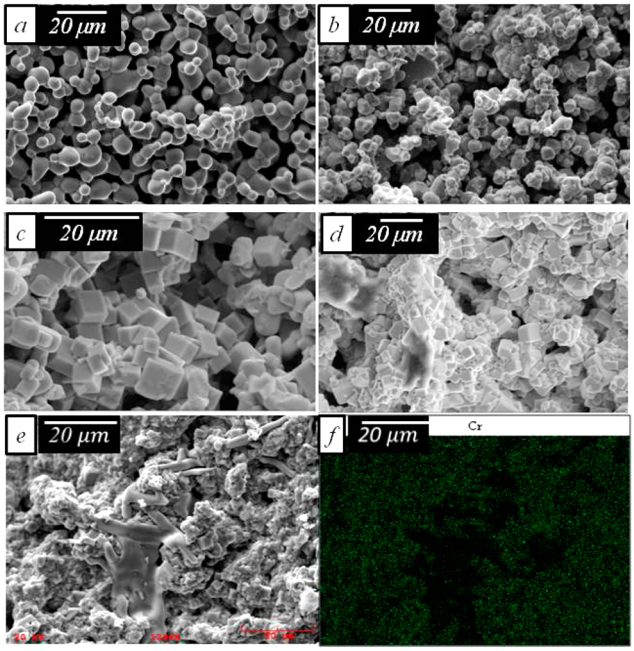

Figure 1. SEM micrographs of unpolished $LaCr_{1-y}Cu_yO_3$ samples for (*a*) y = 0.05, (*b*) y = 0.1, (*c*) y = 0.15, (*d*) y = 0.2, and (*e*) y = 0.3. (*f*) Distribution of Cr corresponding to image *e*.

The SEM images for samples with $y \leq 0.2$ demonstrate these are homogeneous, and EDS analyses were consistent with these having the target stoichiometry. When $y > 0.2$, phase segregation was evident and this became more apparent as the Cu content was further increased. As illustrated in Figure 1*e* the y = 0.3 sample contained areas that appear to have melted, and EDS analysis, Figure 1*f*, demonstrated such areas were Cr poor, suggesting CuO segregation had occurred. It seems the solubility limit for $LaCr_{1-y}Cu_yO_3$ is around y = 0.2. Further evidence for this, from SXRD measurements, will be described below. Previously, Jitaru et al.[38] and Jin et al.[24] reported the preparation of Ni-, Cu-, and Zn-doped oxides with $LaCr_{1-y}B_yO_3$ with y up to 0.5; critically they did not present SEM or structural information for samples with y above 0.2. Presumably they may have encountered the same phase separation observed here.

Crystal Structure of Solid Solution Series $LaCr_{1-y}Cu_yO_3$. The SXRD patterns for the doped $LaCr_{1-y}Cu_yO_3$ ($0 \leq y \leq 0.3$) oxides contained a number of well-resolved *M*-, *R*-, and *X*-point reflections, associated with the presence of in-phase and out-of-phase tilting of the corner-sharing octahedra. Diffraction data were well fitted with an orthorhombic model in space group *Pbnm*, tilt system ($a^-a^-c^+$) in Glazer's notation.[39] This is the same structure seen in undoped $LaCrO_3$.[10−12,24] As a representative example the SXRD pattern for highest single-

dx.doi.org/10.1021/ic402927y | Inorg. Chem. 2014, 53, 2240−2247

phase sample, $LaCr_{0.8}Cu_{0.2}O_3$, is given in Figure 2. The fit of the superlattice reflections is in excellent agreement with the

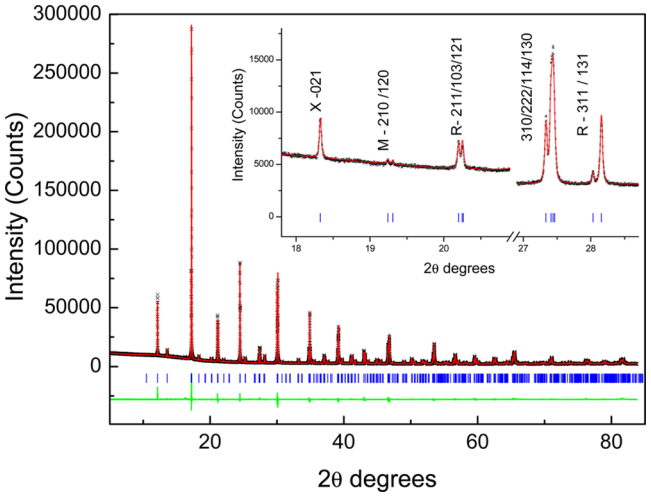

Figure 2. Observed (black symbols), calculated (red line), and difference (green line) SXRD pattern for $LaCr_{0.8}Cu_{0.2}O_3$ at room temperature. (Inset) Weak superlattice reflections indicative of the orthorhombic *Pbnm* space group. Data were collected at λ = 0.82554 Å.

Pbnm model, as illustrated in the inset to Figure 2. The *Pbnm* structure is a superstructure of the cubic perovskite aristotype with $a \approx b = \sqrt{2}a_p$ and $c \approx 2a_p$ where a_p is the equivalent value for cubic structure. A representation of the structure is given in Figure 3, and the refinement parameters for the various single-phase samples are listed in Table 1. In the cubic ABX_3 perovskite structure the larger *A*-type cations are surrounded by 12 anions (*X*, typically oxygen or a halide) in a cuboctahedral coordination and the *B*-type cations are surrounded by six anions in an octahedral arrangement. In the orthorhombic *Pbnm* structure the network of corner-sharing $[BO_6]$ octahedra shows cooperative tilting that may be either in-phase or "plus" rotations that give rise to the *M*-point reflections or out-of-phase or "minus" rotations, giving rise to the *R*-point reflections. In $LaCrO_3$ the tilting of the CrO_6 octahedra reduces the La coordination to an effective 9-coordinate arrangement. As found by Khattak and Cox[40] the refinements shows *a* to be slightly greater than *b*, in contrast to most *Pbnm* structured perovskites. Refinements where the starting values for *a* and *b* were interchanged still converged but with noticeably worse fits, and the observation that $a > b$ is believed to be a consequence of the octahedral tilting. $LaGaO_3$ shows a similar distortion.[41]

That phase segregation that occurs for the Cu-rich oxides with $y > 0.2$ was also evident in the diffraction patterns. The majority of the extra peaks seen in Figure 4 could be indexed to a monoclinic cell in space group *C*2/*c* with a = 4.684 Å, b = 3.4226 Å, c = 5.1288 Å, and β = 99.54° indicative of CuO.[42] That $y \approx 0.2$ is the solubility limit for Cu in $LaCrO_3$ is also evident in the composition dependence of the cell volume, which displays marked deviation from Vegard-type behavior for $y \geq 0.25$ as shown in Figure 5, although the absolute volume expansion is small.

Variable-temperature neutron diffraction data were collected for one example $LaCr_{0.85}Cu_{0.15}O_3$. Above 300 K the data were well fitted to the same orthorhombic model used in the synchrotron study, and the refinement against the 300 K ND data gave extremely similar results to those obtained from refinements against the SXRD data, Table 1. Critically the neutron diffraction data showed no evidence for anomalous displacement parameters that would occur if anion vacancies were formed. This discounts the presence of oxygen vacancies as a means of achieving charge neutrality. Refinement of the Cu/Cr occupancy did not improve the quality of the fit, and the values were in good agreement with the nominal composition; consequently, the Cu:Cr ratio was fixed in the final refinement cycles. Cooling the sample below 300 K resulted in the appearance of additional reflections indicative of antiferromagnetic (AFM) ordering, their intensities progressively increasing on cooling, see Figure 6. The magnetic propagation vector was determined to be k = (0,0,0), and symmetry analysis demonstrated that the spins on the Cr site order in a G-type antiferromagnetic magnetic structure as displayed in the inset of

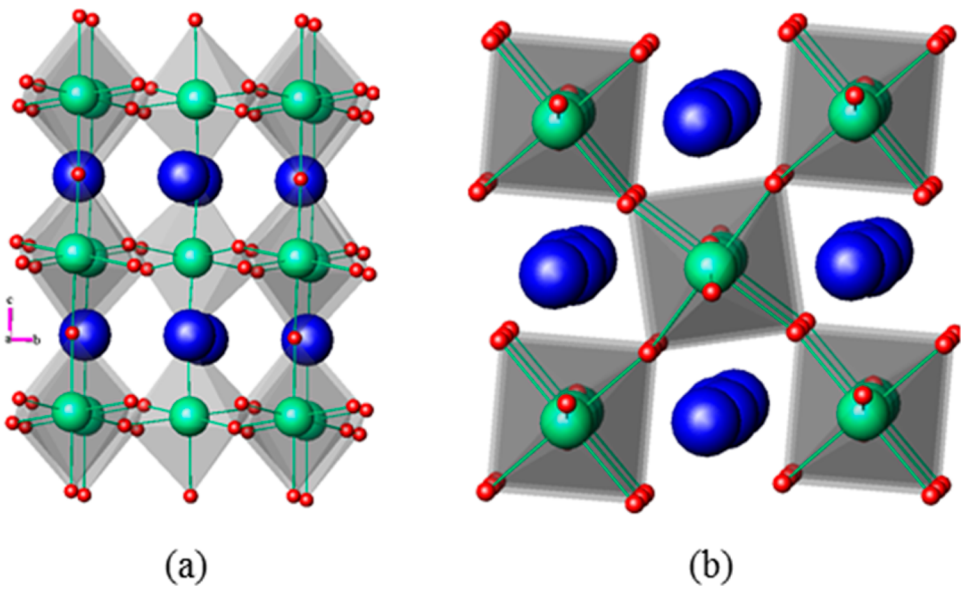

Figure 3. Representation of the orthorhombic structure found for $LaCr_{0.8}Cu_{0.2}O_3$: (a) view from the *a* axis; (b) view from the *c* axis.

dx.doi.org/10.1021/ic402927y | Inorg. Chem. 2014, 53, 2240−2247

Table 1. Selected Structural Parameters for $LaCr_{1-y}Cu_yO_3$ Oxides from Refinements against Synchrotron X-ray or Neutron Diffraction (ND) Data Collected at 295 K

y	0	0.05	0.1	0.15	0.15 (ND)	0.2
t	0.969	0.967	0.966	0.965	0.965	0.963
a (Å)	5.51628(1)	5.52202(1)	5.52043(1)	5.52424(1)	5.52457(10)	5.52510(1)
b (Å)	5.48000(1)	5.48713(1)	5.48726(1)	5.49199(1)	5.49157(12)	5.49358(1)
c (Å)	7.75972(2)	7.76859(1)	7.76822(1)	7.77478(2)	7.77480(14)	7.77682(2)
V (Å^3)	234.5704(9)	235.3869(5)	235.3151(5)	235.8790(9)	235.876(8)	236.0468(9)
R_p (%)	4.26	4.36	3.24	3.41	3.71	2.91
R_{WP} (%)	6.13	6.89	4.24	5.04	4.57	3.9
R_{Bragg}	7.00	3.32	5.22	6.41		5.04
χ^2	7.67	15.77	3.53	10.07	3.15	6.32
La x	0.0040(1)	0.0041(1)	0.0037(1)	0.0037(1)	0.0035(3)	0.0032(1)
La y	0.5192(1)	0.5202(1)	0.5211(1)	0.5214(1)	0.5215(2)	0.5219(1)
La z	0.25	0.25	0.25	0.25	0.25	0.25
B_{iso} (Å^2)	0.92(1)	0.46(1)	0.74(1)	0.87(1)	0.38(3)	0.86(1)
Cr/Cu (0 0 0)						
B_{iso} (Å^2)	0.72(1)	0.35(1)	0.53(1)	0.71(1)	0.41(3)	0.68(1)
O1 x	−0.0604(6)	−0.0684(6)	−0.0690(5)	−0.0681(5)	−0.0667(3)	−0.0708(5)
O1 y	−0.0069(8)	−0.0087(8)	−0.0082(6)	−0.0073(6)	−0.0087(4)	−0.0093(5)
O1 z	0.25	0.25	0.25	0.25	0.25	0.25
B_{iso} (Å^2)	1.32(8)	0.80(5)	1.10(1)	0.92(6)	0.66(3)	1.00(6)
O2 x	0.2308(9)	0.2251(8)	0.2226(5)	0.2244(6)	0.2235(3)	0.2231(5)
O2 y	0.2701(8)	0.2757(6)	0.2770(5)	0.2754(6)	0.2751(3)	0.2785(5)
O2 z	0.0322(4)	0.0361(4)	0.0349(3)	0.0362(3)	0.0354(2)	0.0358(3)
B_{iso} (Å^2)	1.41(6)	0.54(4)	0.95(1)	0.79(4)	0.65(3)	0.98(4)
Cr/Cu−O1 (Å)	1.9688(6)	1.9791(7)	1.9795(5)	1.9802(6)	1.9789(3)	1.9838(6)
Cr/Cu−O2 (Å)	1.969(5)	1.978(4)	1.974(3)	1.976(3)	1.970(2)	1.985(3)
Cr/Cu−O2 (Å)	1.962(5)	1.974(4)	1.979(3)	1.980(3)	1.984(2)	1.975(3)
Cr BVS	3.11	3.03	3.02	3.01	3.02	2.99
Cu BVS	3.20	3.11	3.12	3.11	3.11	3.08
+ tilt (deg)	4.49	2.94	3.09	2.91	5.89	3.26
− tilt (deg)	9.51	10.13	10.18	10.11	11.00	10.32
Δd	1.62×10^{-5}	7.37×10^{-6}	9.46×10^{-6}	5.73×10^{-6}	5.13×10^{-5}	3.03×10^{-5}

[a]The Cr and Cu are disordered at (000). BVS calculations assume Cr^{3+} and Cu^{3+}. t is the tolerance factor and Δ d is the octahedral distortion.

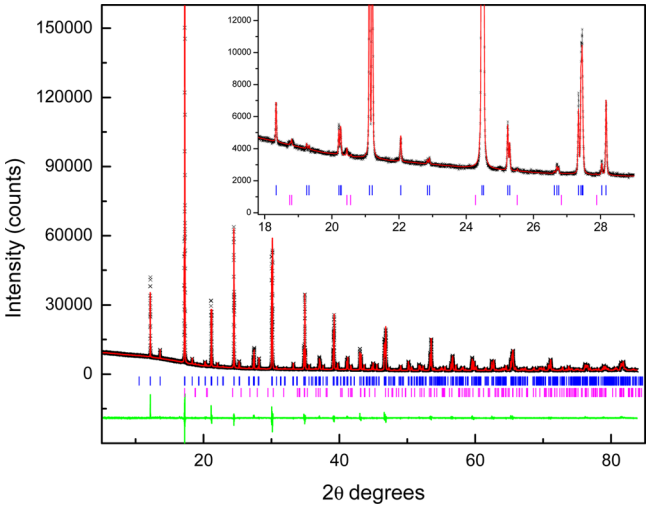

Figure 4. . Observed (black symbols), calculated (red line), and difference (green line) SXRD pattern for $LaCr_{0.7}Cu_{0.3}O_3$ at room temperature. (Inset) Presence of trace amounts of CuO impurity. Upper blue markers are for the perovskite phases in *Pbnm*, and lower, magenta bars, are for CuO.

Figure 7, which shows the Rietveld profiles for the sample at 3 K. This is the same magnetic structure found in undoped $LaCrO_3$.

Addition of Cu to $LaCrO_3$ may affect the structure through either size or electronic effects. There are three possible scenarios to achieve charge balance; the Cu occurs as Cu^{2+} requiring either partial oxidation of Cr to Cr^{4+} or formation of anion vacancies. The third possibility is the Cu is present as Cu^{3+}. The presence of the Jahn−Teller active Cu^{2+} ions with $3d^9$ may result in oxidation of the Cr^{3+} $3d^3$ ($t_{2g}^3e_g^0$) to Cr^{4+} $3d^2$ ($t_{2g}^2e_g^0$), which is also susceptible to a JT-type distortion. The presence of JT active cations may distort the BO_6 octahedra. Tseggai et al.[7] reported a minor increase in the octahedral distortion is present in the Mn^{3+}-substituted oxides $LaCr_{1-y}Mn_yO_3$, reflecting the JT activity of the Mn^{3+} cation. The octahedral distortion can be quantified from the anisotropy in the individual B−O bond lengths as $\Delta d = 1/6 \sum_{n=1,...6}[(dn - d)/d]$,[22] where d_n is the individual B−O bond distance and d is the average of these distances.[43] The observed Δd values are extremely small, and there is no evidence for a systematic change in the distortion as the Cu content was increased in $LaCr_{1-y}Cu_yO_3$ (Table 1). This suggests either there is a lack of coherence in the distortion of the BO_6 octahedra as a consequence of the random distribution of the Cu^{2+} and Cr^{4+} in the structure or that Cu is present as Cu^{3+}.

Another effect of chemical substitution is that it alters the effective size of the B-site cation that can lead to a change in the tilting of the corner-sharing BO_6 octahedra. Such tilting is caused by the mismatch in size between the cations on the A

dx.doi.org/10.1021/ic402927y | Inorg. Chem. 2014, 53, 2240−2247

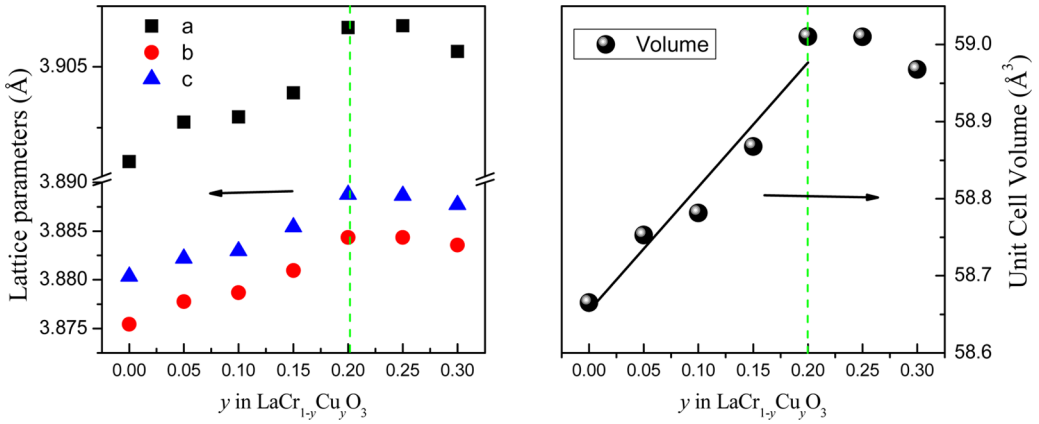

Figure 5. Composition dependence of the lattice parameters (left) and unit cell volume (right) from SXRD refinements for $LaCr_{1-y}Cu_yO_3$. All parameters are normalized ($a/\sqrt{2}$, $b/\sqrt{2}$, $c/2$) to the cubic cell for comparison. Solid line is a linear fit to the volume for the five single-phase samples with $y \leq 0.20$. Where not apparent, the errors are smaller than the symbols.

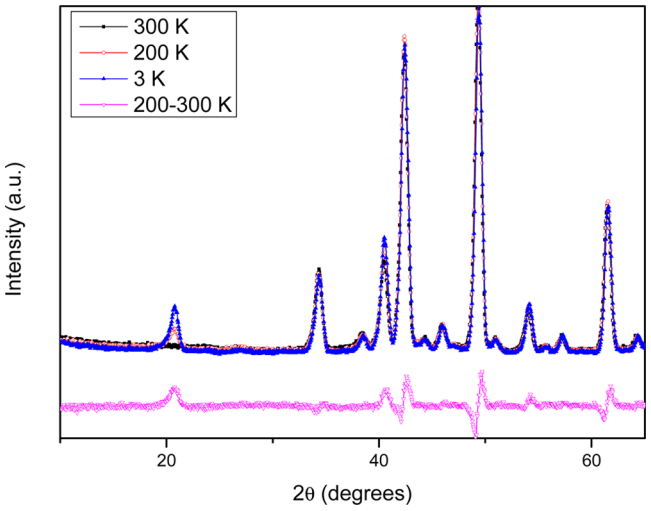

Figure 6. Portions of the observed neutron diffraction profiles for $LaCr_{0.85}Cu_{0.15}O_3$. Lower trace illustrates the difference between the patterns at 200 and 300 K illustrating the growth of the magnetic reflections.

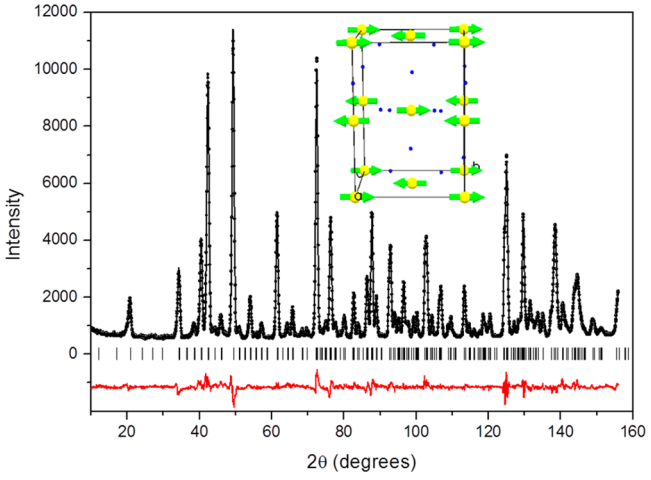

Figure 7. Rietveld refinement plot of the NPD data for $LaCr_{0.85}Cu_{0.15}O_3$ at 3 K. (Inset) Antiferromagnetic G-type structure occurring at the Cr sublattice.

and *B* sites, and its presence is often predicted using the tolerance factor (t) expressed as $t = (r_A + r_O)/\sqrt{2}(r_B + r_O)$, where r_A, r_B, and r_O are the ionic radii of the respective ions in ABO_3. Addition of y mol of Cu^{2+} with ionic radius 0.73 Å will produce y mol of Cr^{4+} (0.55 Å) and $(1 - 2y)$ mol of Cr^{3+} (0.615 Å) will remain at the *B* site.[44] For such an arrangement, the tolerance factor decreases from 0.969 in $y = 0$ to 0.964 in $y = 0.2$. This is expected to result in a small increase in the magnitude of the tilts. The tolerance factor will increase slightly if the Cu is present as Cu^{3+}, which has an ionic radius of 0.54 Å; from 0.969 to 0.976 for $y = 0.2$. Such an arrangement would result in a very small decrease in the tilts.

The orthorhombic *Pbnm* structure is characterized by two independent octahedral tilts, ψ and φ, where ψ is an out-of-phase tilt about the pseudocubic 110 axes and φ is an in-phase tilt about the pseudocubic 001 axis. The octahedral tilt angles in orthorhombic *Pbnm* perovskites can be obtained from the displacement of the O2 oxygen atoms from (1/4 1/4 0) to (1/4−u 1/4+v w). The out-of-phase tilting is estimated by tan $\psi = 4\delta$, where $\delta = (u + v)/2$. The in-phase tilt is estimated by the average of tan $\varphi = 4\sqrt{2}\,w$ and tan $\varphi = 2\sqrt{2}\,x$, where x is the coordinate of the O1 anions.[45,46] There were no noticeable trends in the tilts with increasing Cu content, and the calculated values of these are listed in Table 1. This suggests that the tolerance factor is approximately constant across the series; however, this will occur irrespective of the Cu oxidation state.

Although none of the changes in the structure are sufficiently diagnostic to identify the oxidation state distribution, the bond valence sum calculation shown in Table 1 favors formation of Cu^{3+}, and this is verified by X-ray spectroscopy below. The possibility that charge balance is achieved through formation of oxygen vacancies according to the formula $La^{3+}Cr_{1-y}^{3+}Cu_x^{2+}O_{3-0.5y}$ is discounted from the neutron diffraction measurements.

XANES. The oxidation states of Cr and Cu cations can be established from analyzing the L-edge XANES spectra. The results from the TEY and TFY measurements were similar, confirming the TEY measurements are representative of the bulk material. The Cr L-edge XANES spectra are illustrated in Figure 8a. The L-edge corresponds to the transition of a 2p electron into unoccupied 3d and 4s states (with the 2p-to-3d transition being 50× more probable). The L-edge consists of two major features corresponding to the L_3 edge ($2p_{3/2}$ final state) and L_2 edge ($2p_{1/2}$ final state). In general, the line shape

dx.doi.org/10.1021/ic402927y | Inorg. Chem. 2014, 53, 2240−2247

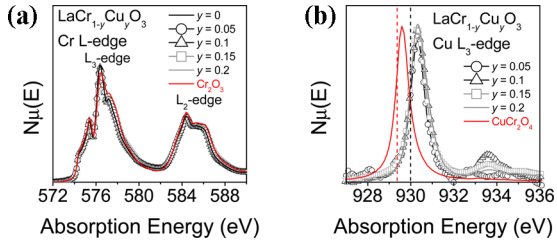

Figure 8. (a) Cr L-edge and (b) Cu L_3-edge XANES spectra of $LaCr_{1-y}Cu_yO_3$ ($0 \leq y \leq 0.2$). Dashed lines in b corresponds to the Cu L_3-edge absorption edge energies of Cu^{2+} (red) and Cu^{3+} (black) species. All spectra were collected in TEY mode.

and absorption edge energy of the Cr L-edge is sensitive to the Cr oxidation state, particularly in Cr^{3+} and Cr^{4+} systems.[47−49] The line shapes of the Cr L-edge spectra of $LaCrO_3$ are similar to that of Cr_2O_3, confirming the presence of Cr^{3+} cations. That the line shape does not change with increasing x in the $LaCr_{1-x}Cu_xO_3$ solid solution indicates that the oxidation state of Cr cations remains +3. Formation of Cr^{4+} should result in development of a high-energy shoulder, similar to that observed in the $La_{1-y}Sr_yCrO_3$ series.[47]

The oxidation state of Cu cations was confirmed by analysis of the Cu L_3 edge (Figure 8b). For both Cu^{2+} and Cu^{3+} systems, the Cu L_3-edge line shape consists of an intense, single white line due to the $3d^9$ (Cu^{2+}) and $3d^8$ (Cu^{3+}) electronic configurations.[50−52] Due to the $3d^{10}$ configuration of Cu^0 and Cu^{1+} species, the $2p_{3/2}$-to-4s transition dominates the L-edge, resulting in a relatively broad, low-intensity line shape.[52] Absorption edge energies are typically used to distinguish between the two oxidation states, with Cu^{3+} species having a higher Cu L_3-edge absorption edge energy.[50−52] In general, the Cu L_3-edge absorption edge energies of Cu-doped $LaCrO_3$ (930.0 eV) are greater than that of $CuCr_2O_4$ (929.3 eV), consistent with Cu having an oxidation state greater than +2. Critically, the absorption edge energy does not change with increasing x, demonstrating that the oxidation state of Cu does not change with increased doping. The XANES analysis, therefore, supports the presence of trivalent Cr and Cu throughout the $LaCr_{1-x}Cu_xO_3$ series, rather than the alternate Cr^{4+}/Cu^{2+} configuration. The Cu L_3-edge spectra also display a feature near 934 eV that is most likely a final state effect due to a ligand-to-metal charge transfer shakeup process caused by excitation of ligand electrons into the empty Cu 3d states. Such satellites have been observed in Cu^{2+} ($3d^9$) and Cu^{3+} ($3d^8$) systems.[53]

Magnetism and Electrical Conductivity. Due to the presence of impurity phases in samples with $y > 0.2$, magnetic and electrical conductivity measurements were limited to samples with $y \leq 0.2$. The magnetic susceptibility versus temperature T with an applied magnetic field $H = 1000$ Oe is plotted in Figure 9 for these samples. Data were collected under both field-cooled and zero-field-cooled conditions, and a noticeable branching of the curves occurs for all samples. It is apparent that Cu doping depresses the magnetic transition T_N from near 300 K in $LaCrO_3$ to around 225 K in $LaCr_{0.8}Cu_{0.2}O_3$. Due to the proximity of T_N to room temperature it was not possible to obtain acceptable Curie−Weiss fits to the inverse susceptibility data.

Neumeier and Terashita[54] observed that straightening the Cr−O−Cr bond angle toward 180° enhances the strength of the magnetic exchange in the related $La_{1-x}Sr_xCrO_3$ series. A

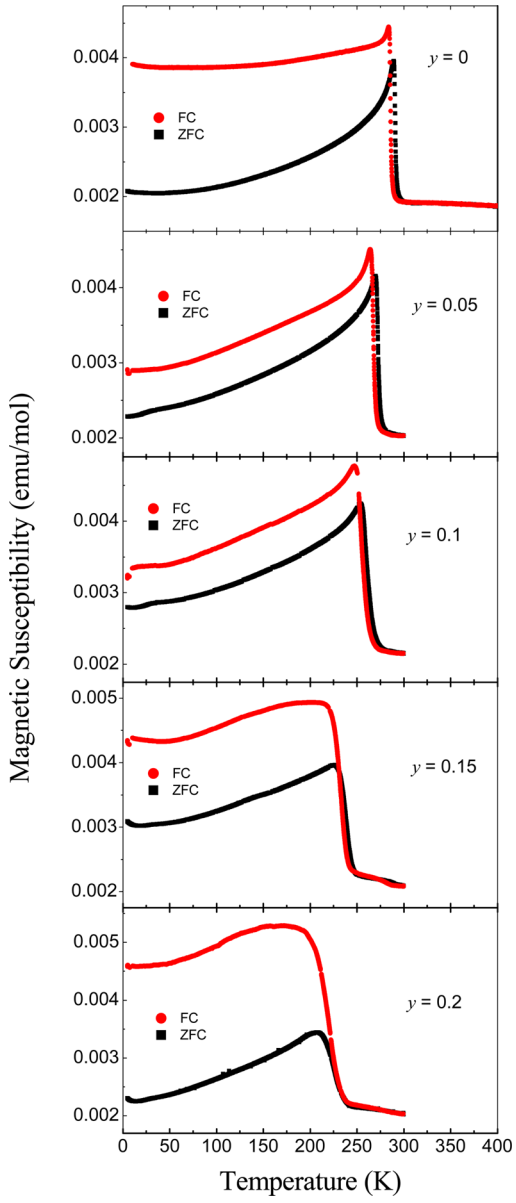

Figure 9. Temperature dependence of the field-cooled and zero-field-cooled magnetic susceptibility for $LaCr_{1-y}Cu_yO_3$.

similar trend is observed here with Cu doping, reducing both T_N and the average Cu−O−Cu angle, see Table 2, and it appears that Cu doping leads to a slight reduction in the Cr−O−Cr bond angles. The Cr−O−Cr bond angles are reduced from 180° by the cooperative tilting of the CrO_6 octahedra; however, such tilting also introduces orbital overlap between the π and the σ bonds. Zhou and co-workers[8] have shown that hybridization of the t_{2g} and e_g (noting the symmetry is actually lower than octahedral) orbitals will lead to a ferromagnetic coupling that will reduce T_N. The correlation between T_N and the bond angles and orbital hydridization will, obviously, be influenced by changes in the d-orbital occupancy, and additional analysis such as DFT calculations would be required to establish the relative importance of such effects.

Magnetization measurements were performed at 5 and 100 K, and the results for all samples were extremely similar. As an example, the hysteresis loop of $LaCr_{0.85}Cu_{0.15}O_3$ is illustrated in Figure 10. As noted above, the oxides have a G-type

dx.doi.org/10.1021/ic402927y | Inorg. Chem. 2014, 53, 2240−2247

Table 2. Refined Cr−O−Cr Bond Angles for $LaCr_{1-y}Cu_yO_3$

Cr−O−Cr bond angle	$y = 0$	$y = 0.05$	$y = 0.10$	$y = 0.15$	$y = 0.2$
Cr(Cu)−O1−Cr(Cu) (deg)	158.4(1)	157.8(2)	157.6(2)	157.9(2)	157.1(2)
Cr(Cu)−O2−Cr(Cu) (deg)	160.7(1)	160.0(2)	159.9(2)	159.9(2)	159.5(2)
average (deg)	159.56	158.9	158.8	158.9	158.3
Néel temperature (K)	290	272	255	229	213

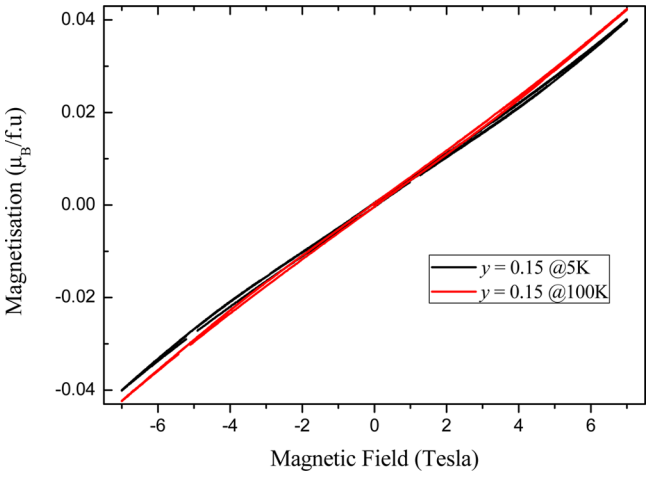

Figure 10. Field dependent magnetization of $LaCr_{0.85}Cu_{0.15}O_3$ at 5 and 100 K.

antiferromagnetic structure, which can lead to weak ferromagnetic behavior as a consequence of a slight canting of the moments away from the antiferromagnetic axis. Alternately, the observed weak ferromagnetic-like response may be attributed to a spin-glass component due to local variation of metal oxidation states, which is also consistent with the divergence of ZFC and FC data (Figure 9). The FM component is too small to be detected by the neutron diffraction data.

Resistivity measurements showed the samples to be semiconductors. As illustrated in Figure 11, for two samples (y = 0.05 and 0.20) there are no features in the temperature dependence of the dc electrical resistivity apparent around T_N, suggesting weak coupling between the charge carriers and the magnetism. The activation energy for these was estimated from a linear fit of $\ln(1/R)$ vs $1/T$ and found to decrease with increasing Cu doping, from 0.23 eV for y = 0.05 to 0.16 eV for y = 0.2. These results are similar to those reported by Jin et al.,[24] who reported an activation energy for $LaCrO_3$ to be 0.25 eV. Addition of Cu increases the conductivity, demonstrating the importance of occupancy of the metal e-type orbitals. As noted above, the occupancy of these also impacts the magnetism through t_2−e hybridization. The importance of the d-electron occupancy in doped $LaCrO_3$ is also evident from studies of $La_{0.9}Sr_{0.1}(Cr_{1-y}Mn_y)O_3$.[55] These results should be considered as a guide to the general behavior and are likely to be influenced by grain boundary effects due to the polycrystalline nature of the samples. Measurements on single crystals or high-quality thin films are necessary to fully investigate the electrical conduction properties of this system; nevertheless, it is clear that Cu doping increases the conductivity, which is a requirement for use of these oxides in SOFC.

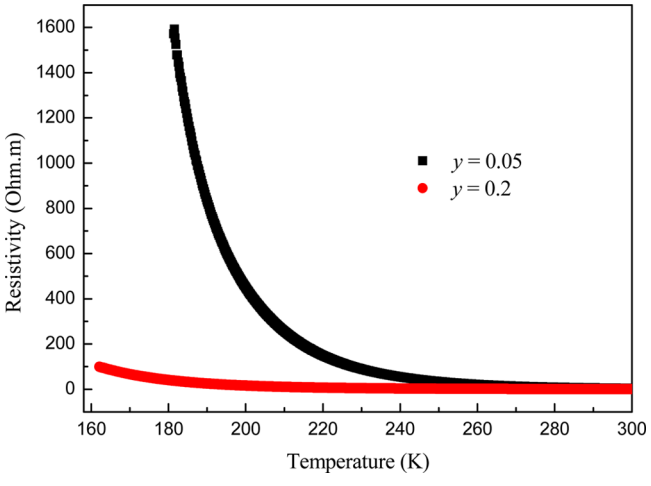

Figure 11. Temperature dependence of resistivity of $LaCr_{1-y}Cu_yO_3$.

CONCLUSION

A series of Cu-doped oxides of the type $LaCr_{1-y}Cu_yO_3$ has been prepared using solid-state methods. Using such methods the solubility limit of Cu was found to be around y = 0.2, with attempts to prepare more heavily doped samples resulting in phase separation. The structures of the samples were established by Rietveld refinements against synchrotron X-ray powder diffraction data that revealed the oxides are all orthorhombic in space group *Pbnm*. XANES measurements at the Cr and Cu L-edges demonstrates both cations to be trivalent. Magnetic measurements demonstrate the oxides to be antiferromagnetic with T_N reducing as the Cu content increased. The samples are semiconductors, and the behavior of these at high temperatures appropriate for operation of SOFCs is worthy of investigation.

ASSOCIATED CONTENT

Supporting Information

Tables of variable-temperature neutron diffraction refinements. This material is available free of charge via the Internet at http://pubs.acs.org.

AUTHOR INFORMATION

Corresponding Author

*Phone: +61 2 9351 2742. Fax: + 61 2 9351 3329. E-mail: B.Kennedy@chem.usyd.edu.au.

Notes

The authors declare no competing financial interest.

ACKNOWLEDGMENTS

This work was partially supported by the Australian Research Council. This work was, in part, performed at the powder diffraction and soft X-ray beamlines at the Australian Synchrotron with the assistance of Drs. Helen Brand and Lars Thomsen.

REFERENCES

(1) Minh, N. Q. *J. Am. Ceram. Soc.* **1993**, *76*, 563−588.
(2) Fergus, J. W. *Solid State Ion.* **2004**, *171*, 1−15.

(3) Jacobson, A. J. *Chem. Mater.* **2010**, *22*, 660−674.
(4) Steele, B. C.; Heinzel, A. *Nature* **2001**, *414*, 345−352.
(5) Weinberg, I.; Larssen, P. *Nature* **1961**, *192*, 445−446.
(6) Koehler, W. C.; Wollan, E. O. *J. Phys. Chem. Solids* **1957**, *2*, 100−106.
(7) Tseggai, M.; Nordblad, P.; Tellgren, R.; Rundlof, H.; Andre, G.; Bouree, F. *J. Alloys Compd.* **2008**, *457*, 532−540.
(8) Zhou, J. S.; Alonso, J. A.; Pomjakushin, V.; Goodenough, J. B.; Ren, Y.; Yan, J. Q.; Cheng, J. G. *Phys. Rev. B* **2010**, *81*, 214115.
(9) Martinelli, A.; Ferretti, M.; Cimberle, M. R.; Ritter, C. *Mater. Res. Bull.* **2011**, *46*, 190−193.
(10) Geller, S. *Acta Crystallogr.* **1957**, *10*, 243−248.
(11) Hashimoto, T.; Tsuzuki, N.; Kishi, A.; Takagi, K.; Tsuda, K.; Tanaka, M.; Oikawa, K.; Kamiyama, T.; Yoshida, K.; Tagawa, H. *Solid State Ionics* **2000**, *132*, 181−188.
(12) Oikawa, K.; Kamiyama, T.; Hashimoto, T.; Shimojyo, Y.; Morii, Y. *J. Solid. State Chem.* **2000**, *154*, 524−529.
(13) Geller, S.; Raccah, P. M. *Phys. Rev.* **1970**, *2*, 1167−1172.
(14) Ruiz, J. S.; Anthony, A. M.; Foex, M. *C. R. Seances Acad. Sci., Ser. B* **1967**, *264*, 1271−1274.
(15) Hofer, H. E.; Kock, W. F. *J. Electrochem. Soc.* **1993**, *140*, 2889−2894.
(16) Akashi, T.; Maruyama, T.; Goto, T. *Solid State Ionics* **2003**, *164*, 177−183.
(17) Meadowcroft, D. *Energy Convers.* **1968**, *8*, 185−190.
(18) Mori, M.; Hiei, Y.; Yamamoto, T. *J. Am. Ceram. Soc.* **2001**, *84*, 781−786.
(19) Sakai, N.; Yokokawa, H.; Horita, T.; Yamaji, K. *Int. J. Appl. Ceram. Technol.* **2004**, *1*, 23−30.
(20) Zhu, W.; Deevi, S. *Mater. Sci. Eng.: A* **2003**, *348*, 227−243.
(21) Minh, N. Q.; Takahashi, T. *Science and technology of ceramic fuel cells*; Elsevier: New York, 1995.
(22) Karim, D.; Aldred, A. *Phys. Rev. B* **1979**, *20*, 2255−2263.
(23) Yasuda, I.; Hikita, T. *J. Electrochem. Soc.* **1993**, *140*, 1699−1704.
(24) Jin, F. X.; Endo, T.; Takizawa, H.; Shimada, M. *J. Solid. State Chem.* **1994**, *113*, 138−144.
(25) Yamamoto, S.; Takeda, Y. In *Electrical Conductivity of Alkaline Earth Metal (Mg, Ca, Sr) Doped Lanthanum Chromites Masashi Mori, Toru Yamamoto, Hibiki Itoh, Toshio Abe Central Research Institute for Electric Power Industry, Nagasaka/Japan*, 1st European Solid Oxide Fuel Cell Forum, 1994; European SOFC Forum: 1994; p 465.
(26) Devi, P. S.; Rao, M. S. *J. Solid. State Chem.* **1992**, *98*, 237−244.
(27) Anderson, H. U., Fabrication and property control of $LaCrO_3$ based oxides. In *Processing of Crystalline Ceramics*; Plenum Press: New York, 1978; pp 469−477.
(28) Bents, U. H. *Phys. Rev.* **1957**, *106*, 225−230.
(29) Sundaresan, A.; Tholence, J.; Maignan, A.; Martin, C.; Hervieu, M.; Raveau, B.; Suard, E. *Eur. Phys. J. B: Condens. Matter Complex Syst.* **2000**, *14*, 431−438.
(30) Zhang, Z.; Kennedy, B. J.; Howard, C. J.; Carpenter, M. A.; Miiller, W.; Knight, K. S.; Matsuda, M.; Miyake, M. *Phys. Rev. B* **2012**, *85*, 174110.
(31) Kennedy, B. J.; Saines, P. J.; Zhou, Q.; Zhang, Z.; Matsuda, M.; Miyake, M. *J. Solid State Chem.* **2008**, *181*, 2639−2645.
(32) Wallwork, K. S.; Kennedy, B. J.; Wang, D. *AIP Conf. Proc.* **2007**, *879*, 879−882.
(33) Howard, C.; Hunter, B. *RIETICA. A computer program for Rietveld analysis of X-ray and neutron powder diffraction patterns*; Lucas Heights Research Laboratories: Syndey, 1998; 1−27.
(34) Liss, K. D.; Hunter, B.; Hagen, M.; Noakes, T.; Kennedy, S. *Physica B* **2006**, *385−86*, 1010−1012.
(35) Larson, A. C.; von Dreele, R. B. General Structure Analysis System (GSAS). *Los Alamos National Laboratory Report No LAUR 86-748*; Los Alamos National Laboratory: Los Alamos, NM, USA, 2000.
(36) Cowie, B. C. C.; Tadich, A.; Thomsen, L. *AIP Conf. Proc.* **2010**, *1234*, 307−310.
(37) Ravel, B.; Newville, M. *J. Synchrotron Radiat.* **2005**, *12*, 537−541.
(38) Jitaru, I.; Berger, D.; Fruth, V.; Novac, A.; Stanica, N.; Rusu, F. *Ceram. Int.* **2000**, *26*, 193−196.
(39) Glazer, A. M. *Acta Crystallogr., Sect. B* **1972**, *28*, 3384−3392.
(40) Khattak, C. P.; Cox, D. E. *Mater. Res. Bull.* **1977**, *12*, 463−471.
(41) Howard, C. J.; Kennedy, B. J., 1999, *11*, 3229-3236.
(42) Yang, B.; Tranquada, J.; Shirane, G. *Phys. Rev. B* **1988**, *38*, 174−178.
(43) Lufaso, M. W.; Woodward, P. M. *Acta Crystallogr., Sect. B: Struct. Sci.* **2004**, *60*, 10−20.
(44) Shannon, R. D. *Acta Crystallogr. A* **1976**, *32*, 751−767.
(45) Kennedy, B. J.; Howard, C. J.; Chakoumakos, B. C. *J. Phys.: Condes. Matter* **1999**, *11*, 1479−1488.
(46) Kennedy, B. J.; Qasim, I.; Reynolds, E.; Tan, T.-Y.; Zhou, Q. *Aust. J. Chem.* **2012**, *65*, 229−235.
(47) Sarma, D. D.; Maiti, K.; Vescovo, E.; Carbone, C.; Eberhardt, W.; Rader, O.; Gudat, W. *Phys. Rev. B* **1996**, *53*, 13369−13373.
(48) Yokobori, T.; Okawa, M.; Konishi, K.; Takei, R.; Katayama, K.; Oozono, S.; Shinmura, T.; Okuda, T.; Wadati, H.; Sakai, E.; Ono, K.; Kumigashira, H.; Oshima, M.; Sugiyama, T.; Ikenaga, E.; Hamada, N.; Saitoh, T. *Phys. Rev. B* **2013**, *87*, 195124.
(49) Ammundsen, B.; Paulsen, J.; Davidson, I.; Liu, R. S.; Shen, C. H.; Chen, J. M.; Jang, L. Y.; Lee, J. F. *J. Electrochem. Soc.* **2002**, *149*, A431−A436.
(50) Hu, Z.; Kaindl, G.; Warda, S. A.; Reinen, D.; de Groot, F. M. F.; Muller, B. G. *Chem. Phys.* **1998**, *232*, 63−74.
(51) Hu, Z.; Golden, M. S.; Ebbinghaus, S. G.; Knupfer, M.; Fink, J.; de Groot, F. M. F.; Kaindl, G. *Chem. Phys.* **2002**, *282*, 451−463.
(52) Grioni, M.; Goedkoop, J. B.; Schoorl, R.; Degroot, F. M. F.; Fuggle, J. C.; Schafers, F.; Koch, E. E.; Rossi, G.; Esteva, J. M.; Karnatak, R. C. *Phys. Rev. B* **1989**, *39*, 1541−1545.
(53) Sarangi, R.; Aboelella, N.; Fujisawa, K.; Tolman, W. B.; Hedman, B.; Hodgson, K. O.; Solomon, E. I. *J. Am. Chem. Soc.* **2006**, *128*, 8286−8296.
(54) Neumeier, J. J.; Terashita, H. *Phys. Rev. B* **2004**, *70*, 214435.
(55) Weber, W. J.; Griffin, C. W.; Bates, J. L. *J. Am. Ceram. Soc.* **1987**, *70*, 265−270.